Earth Syst. Sci. Data Discuss., https://doi.org/10.5194/essd-2019-3
Manuscript under review for journal Earth Syst. Sci. Data
Discussion started: 25 January 2019

Sea-level fingerprints emergent from GRACE mission data

Surendra Adhikari[1], Erik R. Ivins[1], Thomas Frederikse[1], Felix W. Landerer[1], and Lambert Caron[1]

[1]Jet Propulsion Laboratory, California Institute of Technology, Pasadena, CA 91109, USA.

Correspondence: Surendra Adhikari (surendra.adhikari@jpl.nasa.gov)

Abstract. The Gravity Recovery and Climate Experiment (GRACE) mission data set has an important, if not revolutionary, impact on how scientists quantify the water transport on the Earth's surface. The transport phenomena include land hydrology, physical oceanography, atmospheric moisture flux, and climate related changes to the cryosphere. The mass transport observed by the satellite system also includes solid Earth motions caused by, for example, great subduction zone earthquakes and glacial isostatic adjustment (GIA) processes. When coupled with altimetry, this space gravimetry data provides a powerful framework for studying climate related changes on interdecadal time scales, such as ice mass loss and sea-level rise. As the changes in the latter are significant over the past two decades, there is a concomitant self-attraction and loading phenomenon generating ancillary changes in gravity, sea surface, and solid Earth deformation. These generate a finite signal in GRACE and ocean altimetry and it may often be desirable to isolate and remove them for the purpose of understanding, for example, ocean circulation changes and post-seismic viscoelastic mantle flow, or GIA, occurring beneath the sea floor. Here we provide a systematic calculation of sea-level fingerprints of continental (water) mass changes using monthly Release-06 GRACE Level-2 Stokes coefficients for the span April 2002 to August 2016 (*Adhikari et al.*, 2019, https://doi.org/10.7910/DVN/8UC8IR), which result in a set of spherical harmonic coefficients for the time-varying geoid, sea surface, and vertical bedrock motion. A simple sum of the spectra yield monthly maps of the desired field and uncertainties therein. These may be applied for either study of the fields themselves or as fundamental filter components for the analysis of ocean circulation and earthquake related fields, or for improving ocean tide models.

1 Introduction

Geodesists have long understood that the ocean mean sea surface follows the shape of the Earth's geoid (*Rapp*, 1983) and that changes in continental water storage are a source of time-varying gravity (*Lambert and Beaumont*, 1977). The fundamental relationship of changes in land ice, solid Earth, and sea surface height is essential to the study of past and present relative sea-level (e.g., *Peltier*, 1982; *Clark et al.*, 2002; *Tamisiea*, 2011). Our recent gain in confidence for monitoring the geographic locations and amplitudes of both seasonal and supraseasonal changes in global glacier and ice sheet mass, dating to the beginning of the radar interferometry and altimetry era of the early 1990s (e.g., *Rignot et al.*, 2011; *Shepherd et al.*, 2018), strengthens our ability to effectively harness this information to construct informative models about global sea-level variability (*Spada and Galassi*, 2016; *Larour et al.*, 2017; *Mitrovica et al.*, 2018). The mathematical formalism relating changes in gravitational, rotational, and solid Earth deformation responses to land ice and hydrological mass change has now niched itself into contemporary studies of sea-level change: the prediction of "sea-level fingerprints" caused by self-attraction and loading. Sea-level fingerprints are a consequence of the fact that the water elements being transported laterally between land and oceans carry mass, gravitational attraction, and the ability to change the radial stress at the solid Earth surface. These are characterized as changes in relative sea-level encircling areas of intense ice mass loss such as Patagonia, coastal Alaska, the Amundsen Sea sector of West Antarctica, and the Greenland Ice Sheet (e.g., *Mitrovica et al.*, 2001; *Tamisiea et al.*, 2014; *Riva et al.*, 2010; *Adhikari and Ivins*, 2016).

To date, space gravimetric measurements using GRACE monthly gravity fields and the sub-polar ocean altimetry measurements from TOPEX/Poseidon and Jason each have multiple geophysical signals and respective noise floors that are generally high enough that clear detection of these contemporary land-mass-driven fingerprints in the oceans have remained elusive. However, it is believed that these signals will eventually emerge in these data systems. Such a belief springs, in part, from the fact that amplitudes of internal ocean variability in intra- and interannual mass that GRACE observes are relatively mute in comparison to on-land hydrology, two-way land-to-ocean transport, and secular trends in land ice changes (*Chambers*, 2006; *Chambers and Willis*, 2008; *Watkins et al.*, 2015; *Wiese et al.*, 2016; *Save et al.*, 2016). In fact, *Hsu and Velicogna* (2017) have used ocean-bottom pressure data, in conjunction with space geodetic data, to claim that fingerprints associated with decadal scale on-land mass changes are detected. Furthermore, *Davis and Vinogradova* (2017) have shown that the fingerprints of Greenland ice mass loss have measurable influences on tide gauge records along the eastern coast of the US since the mid-1990s. *Galassi and Spada* (2017) have noted that the influence of a land-mass-induced fingerprint may be reflected in tide gauge records of relative sea-level at the northern Antarctic Peninsula, as there is a distinct change in trend at about the year AD 2000, possibly reflecting increased regional ice mass loss. Each of these observations might be considered both intriguing and preliminary in terms of providing the community with unambiguous detection of sea-level fingerprints.

The effects of the fingerprints are nonetheless important to disentangle from many geophysical and ocean circulation models and data sets. New insights into the regional and global sea-level budgets are sought through explicitly combining ocean altimetry with the space gravimetry information, and a key part of this combination is to account for the details of sea-level fingerprints (e.g., *Rietbroek et al.*, 2012; *Frederikse et al.*, 2018). Consideration of land ice and water-driven fingerprints is also necessary when using geodetic data to search for GIA signals residing at or beneath the sea floor (e.g., *Simon et al.*, 2018) or examining ice loss on land when ocean water surrounds the region, such as in Graham Land of the Antarctic Peninsula (*Ivins et al.*, 2011; *Sterenborg et al.*, 2013). Future applications of sea-level fingerprints in geophysical geodesy should include the study of great earthquakes ($M_w \geq 8.0$) at subduction zones (*Han et al.*, 2016) and at ocean rifts beneath the open ocean (*Han et al.*, 2015), or adjacent to the Antarctic Ice Sheet (*King and Santamaría-Gómez*, 2016).

This paper is dedicated to making available to the general scientific user for the first time, sea-level fingerprint information that can be derived from the Release-06 GRACE Level-2 monthly Stokes coefficients for predicting monthly solutions of change in relative sea-level, geoid height, and bedrock displacement induced by on-land mass changes for the period April

2002 to August 2016. The GRACE mission data set has been instrumental to the study of the Earth's climate system (*Tapley et al.*, 2018), and has helped us resolve numerous long-standing questions in oceanography, hydrology, cryosphere, and geodesy. The GRACE gravity solutions are now employed for providing new insights into changes in ocean circulation (*Landerer et al.*, 2015; *Saynisch et al.*, 2015; *Mazloff and Böning*, 2016). The terrestrial water storage is now rigorously quantified for continents (*Johnson and Chambers*, 2013; *Rodell et al.*, 2015; *Hirschi and Seneviratne*, 2017) as is the global cryospheric mass balance (*Velicogna*, 2009; *Jacob et al.*, 2012; *Ivins et al.*, 2013; *Luthcke et al.*, 2013; *Schrama et al.*, 2014). Land mass change and its exchange with the global oceans, in fact, makes it possible to successfully reconstruct subtle changes in the position of Earth's spin axis on interannual time scales (*Adhikari and Ivins*, 2016), thus providing a confidence on the robustness of GRACE based estimates of global surface mass transport.

2 Key variables and deliverables

Relative sea-level is defined as the height of the ocean water column bounded by two surfaces: solid Earth surface and sea surface. Change in relative sea-level, ΔS, at a geographical location described by colatitude and longitude (θ, ϕ) over the time interval Δt may be expressed as follows:

$$\Delta S(\theta,\phi,\Delta t) = \Delta N(\theta,\phi,\Delta t) - \Delta U(\theta,\phi,\Delta t), \tag{1}$$

where ΔN and ΔU are corresponding changes in sea surface height and bedrock elevation, respectively. Tide gauges provide direct measurements of ΔS, whereas satellite altimetry measures ΔN.

Mass redistributed on Earth's surface provides a direct perturbation to the Earth's gravitational and rotational potentials, causing a corresponding perturbation in the geoid height. Since the geoid height on a realistic Earth does not necessarily have to coincide with the sea surface height, we write

$$\Delta S(\theta,\phi,\Delta t) = \frac{1}{g}\Delta\Phi(\theta,\phi,\Delta t) - \Delta U(\theta,\phi,\Delta t) + \Delta C(\Delta t), \tag{2}$$

where $\Delta\Phi$ is the net perturbation in Earth's surface potential, ΔC is a spatial invariant that explains the discrepancy between the sea surface height and geoid height (*Tamisiea*, 2011), measured with respect to the same reference ellipsoid, and g is the mean gravitational acceleration at Earth's surface. As will be further discussed in Section 3, ΔC is essential to conserve mass. Space-based gravity missions, such as GRACE and GRACE Follow-On (GRACE-FO), provide direct measurements of the non-rotational part of $\Delta\Phi$ (to be defined explicitly in Section 3), as the spacecraft retrieve data in an inertial reference frame.

In geodetic applications, field variables are typically expanded in a spherical-harmonic (SH) domain. Most of the GRACE data processing centers – including the University of Texas Austin's Center for Space Research (CSR), Jet Propulsion Laboratory (JPL), and GeoforschungsZentrum Potsdam (GFZ) – provide monthly solutions for normalized SH coefficients of the gravitational potential termed "Stokes coefficients". Stokes coefficient anomalies – the values that deviate from the mean (static) field – can be used to readily retrieve changes in continental water storage or ocean bottom pressure. The goal of this paper is to provide Stokes coefficient anomalies (i.e., SH coefficients of $\Delta\Phi$ minus rotational centrifugal potential) associated with the sea-level fingerprint of monthly changes in continental water storage, which are derived from CSR, GFZ, and

JPL GRACE Stokes coefficients themselves. As we shall further clarify below, we provide these new fingerprint coefficients containing the full effects of solid Earth deformation and sea-level adjustment, both with and without rotational feedback. We also provide SH coefficients for change in relative sea-level ΔS and bedrock elevation ΔU. Corresponding coefficients for sea surface height, ΔN, may be retrieved using equation (1) in an SH domain. For brevity, we hereafter drop the Δ symbol and assume that variables imply "change" in respective fields – not the absolute fields – implicitly.

3 The sea-level equation

Here we briefly summarize the fundamental concept and a numerical technique of solving the so-called "sea-level equation". Much of the background and supporting materials may be found, for example, in *Farrell and Clark* (1976), *Mitrovica and Peltier* (1991), *Adhikari et al.* (2016), and *Spada* (2017). Let $L(\theta,\phi,t)$ be the global, mass-conserving, load function so that:

$$L(\theta,\phi,t) = H(\theta,\phi,t)\mathcal{C}(\theta,\phi) + S(\theta,\phi,t)\mathcal{O}(\theta,\phi), \tag{3}$$

where $H(\theta,\phi,t)$ is the change in water equivalent height over the time period t on the continental domain $\mathcal{C}(\theta,\phi)$, and $S(\theta,\phi,t)$ is the corresponding change in relative sea-level on the oceanic domain $\mathcal{O}(\theta,\phi)$. By definition, $\mathcal{C}$ and $\mathcal{O}$ are complementary functions, such that $\mathcal{C} = 1$ and $\mathcal{O} = 0$ for the continents and $\mathcal{C} = 0$ and $\mathcal{O} = 1$ for the oceans.

The net change in continental (water) mass directly affects the relative sea-level, hence conserving mass on a global scale. Such a redistribution of mass on Earth's surface perturbs its gravitational and rotational potentials and further redistributes the ocean mass. The net result of these perturbations is the sea-level fingerprint: a unique spatial pattern of relative sea-level that is consistent with fundamental physical features of a realistic Earth. For a self-gravitating elastically-compressible rotating Earth, we compute sea-level fingerprint by satisfying the following sea-level equation:

$$S(\theta,\phi,t) = E(t) + \frac{1}{g}\Phi(\theta,\phi,t) - U(\theta,\phi,t) - \left\langle \frac{1}{g}\Phi(\theta,\phi,t) - U(\theta,\phi,t) \right\rangle. \tag{4}$$

The physical interpretation of the right-hand side terms are as follows:

- The barystatic term, $E(t)$, directly follows from the mass conservation principle. This spatial invariant describes S that would be resulted in by distributing the net change in continental water storage uniformly over the oceans.

- Changes in the Earth's surface potential, $\Phi(\theta,\phi,t)$, and the solid Earth surface, $U(\theta,\phi,t)$, may be partitioned as follows:

$$\left\{ \begin{array}{c} \Phi(\theta,\phi,t) \\ U(\theta,\phi,t) \end{array} \right\} = \left\{ \begin{array}{c} \Phi_{\rm g}(\theta,\phi,t) + \Phi_{\rm r}(\theta,\phi,t) \\ U_{\rm g}(\theta,\phi,t) + U_{\rm r}(\theta,\phi,t) \end{array} \right\}, \tag{5}$$

  where $\Phi_{\rm g}$ and $U_{\rm g}$ are the respective signals associated with the perturbation in gravitational potential. We may compute $\Phi_{\rm g}$ and $U_{\rm g}$ by convolving L (equation 3) with the respective Green's functions. Similarly, $\Phi_{\rm r}$ and $U_{\rm r}$ are associated with the perturbation in rotational potential. The change in Earth orientation driven by shifts in the inertia tensor cause both solid Earth deformation and sea-level change (*Lambeck*, 1980). The net effects of the change in orientation of Earth's spin axis, thus, provides a "rotational feedback" (e.g., *Milne and Mitrovica*, 1998). We may compute Φ_r and U_r based on the the perturbation in Earth's inertia tensor due to the global surface mass redistribution described by L (equation 3). We define all of the terms appearing in equations (4) and (5) explicitly in Appendix A.

- The last term in equation (4) represents the ocean-averaged value of $(\Phi/g - U)$. This spatial invariant is essential to ensure that the global mean relative sea-level change is same as the barystatic term.

To solve for the sea-level fingerprint in a conventional SH domain (e.g., *Mitrovica and Peltier*, 1991) and isolate useful SH coefficients noted in Section 2, we express equation (4), using equation (5), in the following form:

$$S(\theta,\phi,t) = X(\theta,\phi,t) + Y(\theta,\phi,t) + P(\theta,\phi,t) + Q(\theta,\phi,t) + C(t), \tag{6}$$

where $X = \Phi_\mathrm{g}/g$, $Y = \Phi_\mathrm{r}/g$, $P = -U_\mathrm{g}$, $Q = -U_\mathrm{r}$, and $C = E - < \Phi/g - U >$. By default, we account for the rotational feedback, which when excluded, equation (6) takes a reduced form with $Y = 0$, $Q = 0$, and $C = E - < \Phi_\mathrm{g}/g - U_\mathrm{g} >$. We now multiply both sides of equation (6) by the ocean function, $\mathcal{O}$, to get the following:

$$\hat{S}(\theta,\phi,t) = \hat{X}(\theta,\phi,t) + \hat{Y}(\theta,\phi,t) + \hat{P}(\theta,\phi,t) + \hat{Q}(\theta,\phi,t) + \hat{C}(t), \tag{7}$$

where $\hat{S} = \mathcal{O}S$, $\hat{X} = \mathcal{O}X$, and so on. In the employed spectral methods (Appendix B), we find it more straightforward to solve equation (7) rather than (6). Since all of the right-hand side terms appearing in equation (7) depend on $\hat{S}$ itself (see equations 3 and 4, and Appendix A), we solve the equation recursively until the desired (solution) convergence is achieved. We consider the barystatic sea-level (equation A1) as the starting solution, i.e. $\hat{S} = \hat{E}$ where $\hat{E} = \mathcal{O}E$. Once equation (7) is solved for $\hat{S}$, all of the terms appearing in equation (6) may be retrieved easily.

We expand all of the terms appearing in equations (6) and (7) in the SH domain (cf. equation B1). Inserting these SH expansions into equation (7) and equating the corresponding (degree l, order m) SH coefficients, we find the following for any r-th recursion:

$$\hat{S}^r_{lm} = \hat{X}_{lm}(\hat{S}^{r-1}_{lm}) + \hat{Y}_{lm}(\hat{S}^{r-1}_{lm}) + \hat{P}_{lm}(\hat{S}^{r-1}_{lm}) + \hat{Q}_{lm}(\hat{S}^{r-1}_{lm}) + \hat{C}_{lm}(\hat{S}^{r-1}_{lm}), \tag{8}$$

where $r = 1, 2, ... r_\mathrm{max}$ is the recursion counter, and r_max is the value of r for which the desired convergence is attained. Note that dependence of right-hand side terms on $\hat{S}_{lm}$ itself is explicitly stated. For $r = 1$, we set $\hat{S}^0_{lm} = \hat{E}_{lm}$. Since $\hat{E}_{lm}$ does not depend on $\hat{S}_{lm}$, it does not evolve during the recursion. We define $\hat{E}_{lm}$ (equation B17) and all of other hatted coefficients appearing above (equation B18 and so on) in Appendix B. The hatted coefficients depend on corresponding non-hatted coefficients, which are explicitly defined in equations (B20–B23, B25).

Once we obtain the final solution for $\hat{S}^r_{lm}$ (after iteration $r = r_\mathrm{max}$), denoted for simplicity by $\hat{S}_{lm}$, final solutions for all of the non-hatted (degree p, order q) coefficients are obtained as well. These non-hatted coefficients automatically satisfy the sea-level equation itself (equation 6) in the SH domain, i.e.,

$$S_{pq} = X_{pq}(\hat{S}_{lm}) + Y_{pq}(\hat{S}_{lm}) + P_{pq}(\hat{S}_{lm}) + Q_{pq}(\hat{S}_{lm}) + C_{pq}(\hat{S}_{lm}). \tag{9}$$

Note that all of SH coefficients appearing above are only a function of time t. With final solutions achieved for all of the terms appearing in equation (9), SH coefficients of geoid height change for a self-gravitating Earth are given by $X_{pq}(t)$ and those for a self-gravitating rotating Earth by $[X_{pq}(t)+Y_{pq}(t)]$. Similarly, SH coefficients of bedrock elevation change are given by $-P_{pq}(t)$ for a self-gravitating Earth and by $-[P_{pq}(t)+Q_{pq}(t)]$ for a self-gravitating rotating Earth.

4 GRACE and sea-level fingerprints

Here we give a brief summary of the steps undertaken to develop sea-level fingerprint and complementary data products. First, we note that the GRACE processing centers, including CSR, GFZ, and JPL, have a variety of methods employed to reduce noise, but the system has an inherent resolution limit of about 300 to 400 km in radius at the Earth's surface. Hence, the Stokes coefficients for the potential field provided by the official centers are truncated at a varying degree and order, from 60 to 96. We employ a truncation at degree and order 60, as many months may be much noisier than others.

We use GRACE Level-2 Release-06 data products provided by all three premier (and official) data processing centers (available at ftp://podaac.jpl.nasa.gov/allData/grace/L2/) that are available for the spans April 2002 through August 2016 (CSR and JPL) and January 2003 through November 2014 (GFZ). The Release-06 GSM files represent the total gravity variability due to land surface hydrology, cryospheric changes, episodic seismogenic processes, and GIA. We assume that all mass transport information is contained within the post-processed GSM files in which background models for the mass changes in atmosphere and oceans having periodicities shorter than one month are removed (*Dobslaw et al.*, 2017). GSM data set are also corrected for solid Earth and ocean tides by the processing centers (cf. *Stammer et al.*, 2014; *Bettadpur*, 2018). We also assume continuous transfer of net mass to and from the oceans takes place on all time scales. This includes a trend that supplies the mass term of sea-level rise. To do this correctly, we derive degree 1 coefficients from JPL Release-06 data products following the methods of *Swenson et al.* (2008). We replace degree 2 order 0 coefficients by those derived from satellite laser ranging analysis (*Cheng et al.*, 2011) that are compatible with Release-06 data products (available at ftp://podaac.jpl.nasa.gov/allData/grace/docs/TN-11_C20_SLR.txt). We apply GIA correction coefficient-by-coefficient using the expected values from a Bayesian analysis (*Caron et al.*, 2018), available at https://vesl.jpl.nasa.gov/solidEarth/gia/. Finally, for all coefficients, we remove corresponding 11-year (January 2003 – December 2013) mean values to retrieve Strokes coefficient anomalies.

By combining GSM Stokes coefficient anomalies with GIA and low-degree coefficients as noted above, we may derive corresponding coefficients for land water storage anomalies, $H_{lm}(t)$, as follows (*Wahr et al.*, 1998):

$$H_{lm}(t)=\frac{a\rho_e}{3\rho_w}\frac{2l+1}{1+k_l'}\left\{\exp\left[-\frac{1}{4\,\ln(2)}\left(\frac{l\,r}{a}\right)^2\right]\right\}\left[C_{lm}^{\mathrm{gsm}*}(t)-C_{lm}^{\mathrm{gia}}(t)\right], \tag{10}$$

where ρ_w is the water density, ρ_e is the Earth's mean density, k_l' are the load Love numbers of degree l, a is the Earth's mean surface radius, r is the Gaussian smoothing window, and C_{lm}^{gsm} and C_{lm}^{gia} are the GSM and GIA Stokes coefficient anomalies, respectively. The term enclosed by braces is the Gassian smoothing filter. We consider $r = 300$ km to comply with the so-called gain factors that are used to restore the attenuated signals (detailed below). An asterisk associated with GSM coefficients is meant to imply that these solutions are corrected for more accurate low-degree Stokes coefficients as noted above.

Monthly land water storage fields, $H(\theta,\phi,t)$, may be generated by assembling the coefficients (equation 10) in an SH domain, as in equation (B1). Gaussian smoothing aimed at removing the data noise also attenuates the signals. An appropriate scaling of the fields is therefore essential. For the ice sheet and peripheral glaciers in Greenland, three non-overlapping subdomains of Antarctica, and 15 regions of global glaciers and ice caps, we compare our estimates of average rate of regional mass change during February 2003 through June 2013 with those computed by *Schrama et al.* (2014) and derive the scaling factors – unique for CSR, GFZ, and JPL data products – for each of these 19 cryospheric domains. As for the non-cryospheric continental domains, *Landerer and Swenson* (2012) analyzed monthly land water storage signals obtained from the GRACE observations and the Noah land surface model, simulated within the Global Land Data Assimilation System (GLDAS-Noah), and derived global gridded gain factors. We combine these factors to scale $H(\theta,\phi,t)$ for the entire continents. Our estimates of barystatic time series are comparable to JPL mascon solutions for both trends and seasonal amplitudes (Figure 1).

A detailed description of the scaling may be found in *Adhikari and Ivins* (2016), who used the same recipe to post-process the CSR Release-05 GRACE Level-2 data products for robust reconstruction of interannual variability in position of Earth's spin axis. This gives us extraordinary confidence that the procedure for generating land water storage fields and corresponding fingerprints are not only sound, but highly robust at long wavelengths. The effects of scaling on low-degree SH coefficients of select fields are shown in Figure 2. Our model solutions for sea-level fingerprints (Figure 3) are also robust. Our estimates of relative sea-level, vertical bedrock motion, and geoid height change are consistent with the respective solutions (not shown) computed using a well-validated sea-level solver that operates on an unstructured global mesh (*Adhikari et al.*, 2016).

With this short paper, we provide monthly scaled $H_{lm}(t)$ and two sets of results – with and without rotational feedback – for monthly SH coefficients associated with (see equation 9):

- geoid height change: $[X_{lm}(t) + Y_{lm}(t)]$,
- vertical bedrock motion: $-[P_{lm}(t) + Q_{lm}(t)]$,
- relative sea-level: $S_{lm}(t)$.

The coefficients for sea surface height may be obtained by summing coefficients for bedrock motion and those for relative sea-level (cf. equation 1). One may assemble these coefficients in an SH domain to retrieve the corresponding monthly fields. We also provide uncertainty associated with monthly fields in terms of SH coefficients (not the uncertainty in SH coefficients themselves). Based on the JPL Release-06 (GIA uncorrected) mascon solutions and associated standard errors (*Watkins et al.*, 2015; *Wiese et al.*, 2016), we use a Monte-Carlo approach to generate 5000 ensemble members of monthly land water storage solutions. We apply a unique GIA correction, computed by *Caron et al.* (2018), to each of these ensemble members. We then solve the sea-level equation to derive an equivalent number of solutions for $S(\theta,\phi,t)$, $U(\theta,\phi,t)$ and other fields. Finally, we quantify the standard errors associated with each field, weighted by the likelihood of each GIA model (*Caron et al.*, 2018). Figure 3 shows our estimates of standard errors associated with the trends in land water storage and relative sea-level.

The utility of the fields we provide is that they may be used to rigorously remove from ocean altimetry, bottom-pressure and tide gauge studies those patterns that are attributable to geoid and bedrock motions caused by on-land mass changes. Such

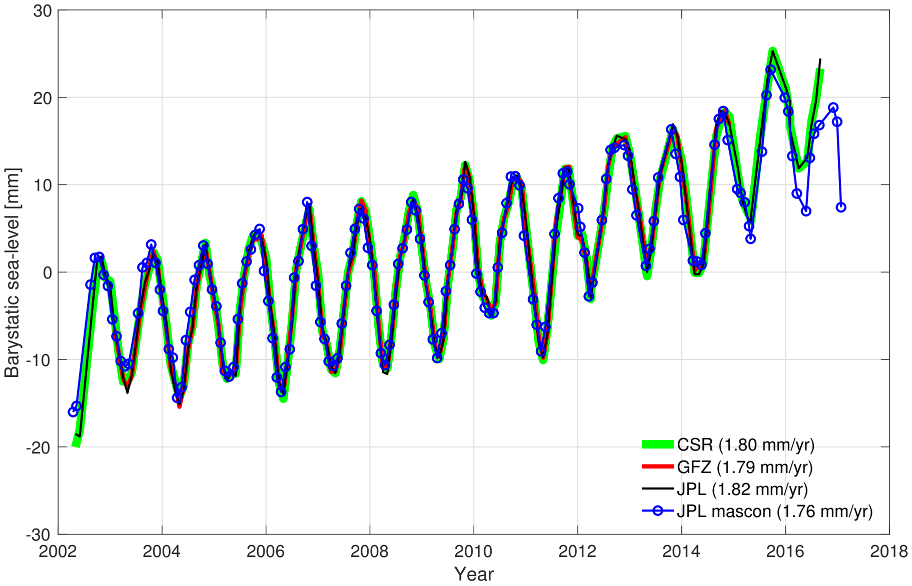

Figure 1. Barystatic sea-level time series computed by summing continental water height changes. Our estimates of trends and seasonal amplitudes for all three data centers are compared to JPL mascon solutions (*Watkins et al.*, 2015). Results are plotted relative to the time means over the period January 2003 through December 2013. Trend values are provided for the period January 2005 through December 2015, except for GFZ solutions (January 2005 to December 2013), for a comparison to the sum of individual mass components (during January 2005 to December 2016) listed in Table 13 of the *WCRP* (2018) report: 1.65 ± 0.23 mm/yr. As an additional point of comparison, *Dieng et al.* (2015) find GRACE-determined mass changes for the barystatic sea-level trend at 2.04 ± 0.08 mm/yr for January 2005 – December 2013 from the mean of CSR, GFZ and JPL Level-2 Release-05 spherical harmonic solutions.

removal is essential for future studies of the patterns of sea-level change owing to internal variability of the climate system which drive changes in ocean density, fresh water fluxes and circulation (e.g., *Bilbao et al.*, 2015; *Fasullo and Nerem*, 2018).

As we supply sea-level fingerprints and complementary data products with and without rotational feedback, we owe the readers some additional words of caution and recommendations. First, from the Eurlerian equations of rotational motion, we solve for the feedback consistently designed for periods longer than 434 days (the period of the Chandler wobble). The rationale is that both the solid and ocean pole tide (*Haubrich and Munk*, 1958) are removed from the satellite solutions for GRACE gravimetry and TOPEX/Poseidon and Jason altimetry on a routine basis (e.g., *Wahr*, 1985; *Desai*, 2002; *Desai and Yuan*, 2006). The improvements in the ocean pole tide, in fact, has been accomplished by many years of assimilation of the altimetric mission data. Hence, at periods near, or less than 434 days, the paths to unambiguously generating solutions to the sea-level equation with centrifugal potential and loading changes from the pole tide are unclear. We might assume that the relevant feedbacks are largely removed as a processing step in rendering Level 1-b and Level 2 GRACE data products. We keep, however, rotational feedback effects of an interannual nature in one set of monthly solutions, and another set of solutions lack these effects. The user of this data should understand the differences, as approaches to using the data to evaluate altimetric

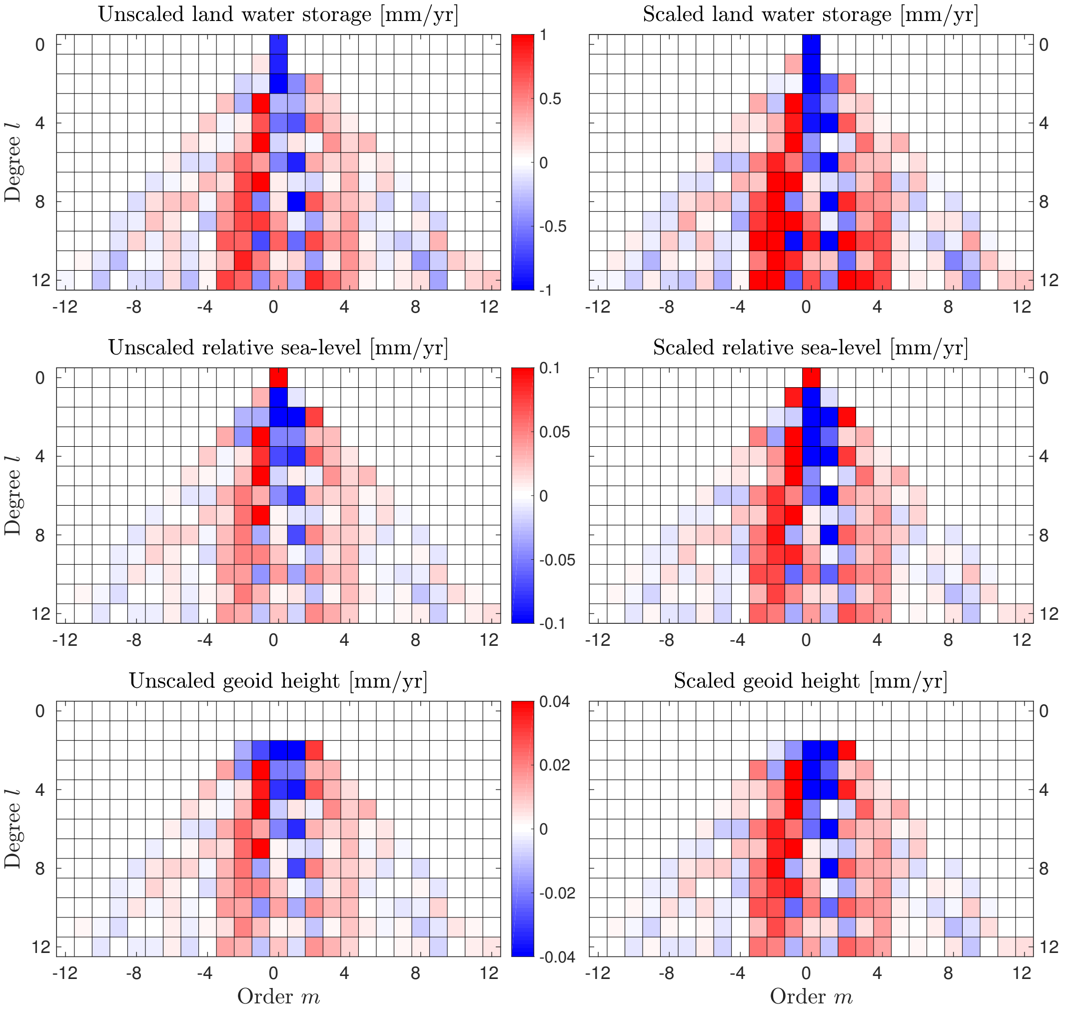

Figure 2. Low-degree spherical harmonic coefficients of select fields for JPL solutions. Shown are average rates of water equivalent height change in land water storage, relative sea-level, and geoid height, for the period April 2002 to March 2016. We show both unscaled (left panel) and appropriately scaled (right panel) solutions (cf. Section 4). Both cases account for the rotational feedback.

time series of order 10 years in length will certainly be interested in using the rotational feedback version for analysis of interannual trend and variability adjacent to Greenland, for example (*Müller et al.*, 2018). Whereas, users focusing on seasonal time scale fingerprints are recommended to employ those coefficients that lack the rotational feedback, as the altimetry and space gravimetry products employed, likely have the sea surface height and gravity effects of the annual polar motion, Chandler wobble, and associated pole tides removed.

It is also worthwhile to note that on time scales of decades the mantle primarily behaves elastically, perhaps with the exception at places where the tectonic history has brought heat, volatiles and changes in mineral structure, such as water or reduced grain size, into the region, thus reducing the effective viscosity to values below about 5×10^{18} Pa s (e.g., *Lange et*

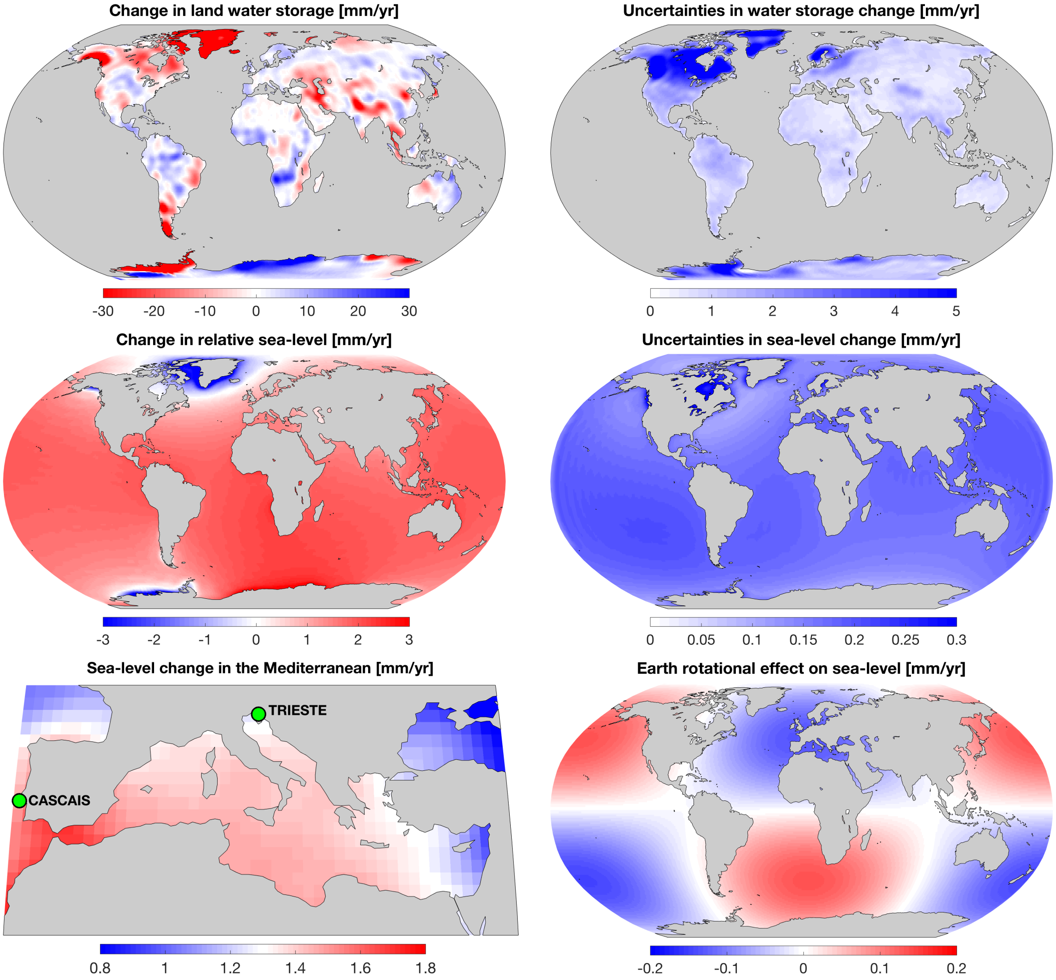

Figure 3. Land load function, sea-level fingerprint, and uncertainties therein for JPL solutions. Average rate of water equivalent height change in land water storage (upper panel) and associated sea-level fingerprint (middle panel) for the period April 2002 to March 2016 are shown with their corresponding 1-σ uncertainties. Maps for sea-level fingerprint and uncertainty are produced by assembling the corresponding spherical harmonic coefficients provided with this article. A zoom-in map of the Mediterranean Sea (bottom left) is meant to highlight the local variability in sea-level fingerprint. The fingerprint-predicted trends for tide gauges at TRIESTE (1.26 ± 0.18 mm/yr) and CASCAIS (1.50 ± 0.17 mm/yr) reflect differences that are comparable to those associated with interdecadal atmospheric pressure trends (0.2 ± 0.2 mm/yr) and the GIA related fingerprint (≈ 0.2 mm/yr) (see *Piecuch et al.* (2016) and *Stocchi and Spada* (2009), respectively). This illustrates one example of the importance of contemporary sea-level fingerprints for tide gauge data analysis and interpretation. Rotational feedback on relative sea-level trend exhibits a degree-2 spherical harmonic pattern (bottom right), and generally accounts for $\approx 10\%$ of the total signal.

al., 2014; *Mitrovica et al.*, 2018; *Nield et al.*, 2018). At such low values of viscosity in the upper mantle, stress relaxation can reduce both the effective influence of gravitational loading and the amplitude of fingerprints. While we acknowledge that this effect is quite difficult to quantify, it should be a second order effect.

5 Conclusions

In this paper we describe a data product that emerges from the Release-06 GRACE Level-2 Stokes coefficients – provided by three official data processing centers namely CSR, GFZ, and JPL – which contain the basic information necessary to create monthly sea-level fingerprints, and these are general enough that they may be employed in reconstructions of vertical bedrock motion, perturbed relative sea surface, and geoid height. We provide spherical harmonic coefficients of each field (relative to the mean determined over the span of January 2003 - December 2013), with and without rotational feedback, and uncertainty therein at monthly interval for the periods April 2002 to August 2016 (CSR and JPL) and January 2003 to November 2014 (GFZ). These coefficients may be readily assembled in a spherical harmonic domain to retrieve the desired fields on a latitude-longitude grid.

A future space altimetry mission (Surface Water and Ocean Topography, or SWOT) is aimed at providing real-time two-dimensional imaging of the sea surface height without the necessity of having to patch together one-dimensional profiles (e.g., *Gaultier et al.*, 2016). In addition to providing higher resolution, this will allow improved accuracy. When coupled to GRACE-FO mapping of gravity changes, we should begin to see the emergence of sea-level fingerprints. Perhaps more importantly, we may begin to more confidently remove a part of the ocean altimetry signal that should not be assimilated into dynamic ocean models: that which is associated with self-gravitation and loading. Here we present the effects of land-based mass transport and rotational effects, both together and separately. Recent appreciation of the effects of solid Earth elastic and viscoelastic response is now receiving increased scrutiny for the potential bias that may be introduced into the altimetry trend record when not accounting for these effects properly (e.g., *Desai et al.*, 2015; *Lickley et al.*, 2018). We have not treated the influences of GIA on rotational deformation and/or the associated axial displacement of the centrifugal potential, although we have employed the GIA model of *Caron et al.* (2018) to analyze GRACE Level-2 for proper representation of the monthly water height equivalent masses. As a consequence, users of the data that we supply here should understand that folding the fingerprints into analyses of any geodetic data, including tide gauges and ocean altimetry, might want to carefully consider that the secular polar motion effects in the Release-06 GRACE Level-2 products (*Wahr et al.*, 2015; *Bettadpur*, 2018) have been removed, and that the sea surface height variability associated with polar drift, annual, and Chandler wobble effect are currently removed from ocean altimetry data in the manner described by *Desai et al.* (2015). This fact allows users to rather straightforwardly remove land mass change related fingerprints from either GRACE, ocean altimetry, tide gauge or GPS-determined vertical land motion data from April 2002 to August 2016 using the monthly spherical harmonic coefficients we supply here as a data product.

6 Data availability

We presently store data in a public repository (https://doi.org/10.7910/DVN/8UC8IR) hosted by Harvard Dataverse (*Adhikari et al.*, 2019). We are working to store these data set also to PODAAC (https://podaac.jpl.nasa.gov/) – NASA's Physical Oceanography Distributed Active Archive Center. There are a total of 890 data files: 133×2 for GFZ and 156×2 each for CSR and JPL. For the given data center, two files are provided for a particular GRACE month: one with Earth's rotational feedback included, and another without, while solving for sea-level fingerprints. File names follow the GRACE naming convention. Solutions

Earth Syst. Sci. Data Discuss., https://doi.org/10.5194/essd-2019-3
Manuscript under review for journal Earth Syst. Sci. Data
Discussion started: 25 January 2019

computed for the CSR data set "GSM-2_2002095-2002120_GRAC_UTCSR_BA01_0600", for example, are stored in files named "SLF*_WITHrotation" and "SLF*_WOUTrotation". We simply replace "GSM" by "SLF" – which denotes "sea-level fingerprints" – and append "_WITHrotation" or "_WOUTrotation" in the end to note whether or not the solutions provided in a particular file account for rotational feedback. Time stamp (in YYYYDoY-YYYYDoY format) and the corresponding data center (5 character string containing CSR, GFZ or JPL) also appear in the file name. The example file considered above contains sea-level fingerprint solutions for the period 95-120 days of year 2002 based on the Stokes coefficients provided by CSR. Header lines 5 and 6 in each file further clarify which data center the solutions correspond to and whether or not Earth's rotational feedback is accounted for. Each data file consists of a total of 18 columns: SH degree l, SH order m, and SH coefficients for land load function H_{lm} (4 columns), relative sea-level S_{lm}(4 columns), geoid height change $[X_{lm}+Y_{lm}]$ (4 columns), and vertical bedrock motion $-[P_{lm}+Q_{lm}]$ (4 columns). For each field, first (last) two columns store cosine (sine) coefficients for our predicted mean and 1-σ uncertainty, respectively. Users should note that the finite degree-0 order-0 harmonic in the monthly SLF files represents the finite mass changes for the global oceans.

Appendix A: Theory of sea-level fingerprint

The fundamental theoretical concept of the so-called sea-level fingerprint is summarized in Section 2. Here we provide explicit mathematical expressions for all of the terms appearing in equation (4).

- The barystatic term is given by

  $$E(t) = -\frac{1}{A_{\mathrm{O}}}\left[a^2\int H(\theta,\phi,t)\mathcal{C}(\theta,\phi)\,\mathrm{d}\mathbb{S}\right], \tag{A1}$$

  where

  $$A_{\mathrm{O}} = a^2\int \mathcal{O}(\theta,\phi)\,\mathrm{d}\mathbb{S} \tag{A2}$$

  is the ocean surface area, a is the Earth's mean radius, and $\mathbb{S}$ is the surface domain of a unit sphere. The term enclosed by brackets in equation (A1) yields the net change in continental water volume.

- Changes in gravitational potential, Φ_{g}, and associated changes in Earth's surface displacement, U_{g}, are obtained by convolving the surface loading function (equation 3) with respective Green's functions, $\mathcal{G}_\Phi$ and $\mathcal{G}_U$, as follows:

  $$\left\{\begin{array}{c}\Phi_{\mathrm{g}}(\theta,\phi,t)\\ U_{\mathrm{g}}(\theta,\phi,t)\end{array}\right\} = a^2\rho_w\int\left\{\begin{array}{c}\mathcal{G}_\Phi(\alpha)\\ \mathcal{G}_U(\alpha)\end{array}\right\}L(\theta',\phi',t)\,\mathrm{d}\mathbb{S}', \tag{A3}$$

  where (θ',ϕ') are the variable coordinates. These variable coordinates at which the loading function is defined are related to (θ,ϕ) at which Φ_{g} and U_{g} are evaluated via the great-circle distance, α, as follows: $\cos\alpha = \cos\theta\cos\theta' + \sin\theta\sin\theta'\cos(\phi'-\phi)$. Green's functions are represented in the Legendre transform domain as follows:

  $$\left\{\begin{array}{c}\mathcal{G}_\Phi(\alpha)\\ \mathcal{G}_U(\alpha)\end{array}\right\} = \frac{3}{4\pi a^2\rho_e}\sum_{l=0}^{\infty}\left\{\begin{array}{c}g\,(1+k_l')\\ h_l'\end{array}\right\}P_l(\cos\alpha), \tag{A4}$$

where P_l are Legendre polynomials (equation B3), and k_l' and h_l' are the load Love numbers.

- Changes in rotational potential, Φ_r, and associated changes in Earth's surface displacement, U_r, follow from the Eulerian theory of rotation (*Lambeck*, 1980):

$$\left\{\begin{array}{c}\Phi_\mathrm{r}(\theta,\phi,t)\\ U_\mathrm{r}(\theta,\phi,t)\end{array}\right\} = \left\{\begin{array}{c}1\\ 0\end{array}\right\}\Lambda_{00}(t)\mathcal{Y}_{00}(\theta,\phi)+\sum_{m=-2}^{2}\left\{\begin{array}{c}(1+k_2)\\ h_2/g\end{array}\right\}\Lambda_{2m}(t)\mathcal{Y}_{2m}(\theta,\phi), \tag{A5}$$

where $\mathcal{Y}_{lm}$ are degree l order m spherical harmonics (equation B2), Λ_{lm} are SH coefficients of perturbation in rotational potential, and k_2 and h_2 are degree-2 tidal Love numbers. We may express changes in rotational potential in terms of changes in Earth's rotation parameters, moment of inertia, and hence surface loading function. Considering leading-order terms only, we get the following non-zero coefficients (*Milne and Mitrovica*, 1998):

$$\left\{\begin{array}{c}\Lambda_{21}(t)\\ \Lambda_{2-1}(t)\end{array}\right\} = -\frac{1}{\sqrt{15}}a^2\Omega^2\left(\frac{\Omega(1+k_2')}{\mathbb{A}\sigma_0}\left[\frac{-4\pi}{\sqrt{15}}\rho_w a^4\left\{\begin{array}{c}L_{21}(t)\\ L_{2-1}(t)\end{array}\right\}\right]\right), \tag{A6}$$

and

$$\left\{\begin{array}{c}\Lambda_{00}(t)\\ \Lambda_{20}(t)\end{array}\right\} = \left\{\begin{array}{c}2/3\\ -2/(3\sqrt{5})\end{array}\right\}a^2\Omega^2\left(-\frac{1+k_2'}{\mathbb{C}}\left[\frac{8\pi}{3}\rho_w a^4\left\{L_{00}(t)-\frac{1}{\sqrt{5}}L_{20}(t)\right\}\right]\right), \tag{A7}$$

where Ω is the Earth's mean rotational velocity, $\mathbb{A}$ and $\mathbb{C}$ are the mean equatorial and polar moment of inertia, respectively, σ_0 is the so-called Chandler wobble frequency, and L_{lm} are SH coefficients of the surface loading function (equation B11). Note that the terms inside brackets represent for changes in Earth's moment of inertia: $\Delta\boldsymbol{I}_{11}$ and $\Delta\boldsymbol{I}_{22}$ (equation A6) and $\Delta\boldsymbol{I}_{33}$ (equation A7). Similarly, the terms enclosed by outer parentheses represent for Earth's rotation parameters: polar motion $(\boldsymbol{m}_1,\boldsymbol{m}_2)$ (equation A6) and change in length of day $\boldsymbol{m}_3$ (equation A7).

- The ocean-averaged term in equation (4), denoted by $\langle * \rangle$, may be written as follows:

$$\left\langle\frac{1}{g}\Phi(\theta,\phi,t)-U(\theta,\phi,t)\right\rangle = \frac{1}{A_\mathrm{O}}\left[a^2\int\left\{\frac{1}{g}\Phi(\theta,\phi,t)-U(\theta,\phi,t)\right\}\mathcal{O}(\theta,\phi)\,\mathrm{d}\mathbb{S}\right]. \tag{A8}$$

When rotational feedback is excluded, Φ and U should be replaced by Φ_g and U_g, respectively.

Appendix B: Spectral methods for sea-level equation

B1 Primer

- ***Spherical harmonics.*** For brevity, we define $\omega=(\theta,\phi)$ and drop explicit dependence of a function on time so that $f(\theta,\phi,t)\equiv f(\omega)$. Any square-integrable function $f(\omega)$ can be expanded as the infinite sum of SHs as follows:

$$f(\omega)=\sum_{l=0}^{\infty}\sum_{m=-l}^{l}f_{lm}\mathcal{Y}_{lm}(\omega)\equiv\sum_{lm}f_{lm}\mathcal{Y}_{lm}(\omega), \tag{B1}$$

where f_{lm} are SH coefficients and $\mathcal{Y}_{lm}(\omega)$ are (real) normalized SHs of degree l and order m. These SHs may be expressed in terms of associated Legendre polynomials, $\mathcal{P}_{l|m|}$, as follows:

$$\mathcal{Y}_{lm}(\omega) = \sqrt{(2-\delta_{0m})(2l+1)\frac{(l-|m|)!}{(l+|m|)!}}\,\mathcal{P}_{l|m|}(\cos\theta)\begin{cases}\cos(m\phi) & \text{if } m \geq 0\\ \sin(|m|\phi) & \text{if } m < 0\end{cases}. \tag{B2}$$

where δ_{0m} is the Kronecker delta. For $x \in [-1,1]$ and $m \geq 0$, polynomials $\mathcal{P}_{lm}(x)$ are given by

$$\mathcal{P}_{lm}(x) = (1-x^2)^{m/2}\frac{\mathrm{d}^m\mathcal{P}_l(x)}{\mathrm{d}x^m},$$

where

$$\mathcal{P}_l(x) = \frac{1}{2^l\, l!}\frac{\mathrm{d}^l(x^2-1)^l}{\mathrm{d}x^l} \tag{B3}$$

are the Legendre polynomials. This definition of SHs and their normalization are consistent with those employed for GRACE data generation and processing (*Bettadpur*, 2018).

- ***SH addition theorem.*** It is useful to note here that the following relationship holds:

$$\mathcal{P}_l(\cos\alpha) = \frac{1}{2l+1}\sum_{m=-l}^{l}\mathcal{Y}_{lm}(\omega)\mathcal{Y}_{lm}(\omega'), \tag{B4}$$

where α once again is the great-circle distance between coordinates ω and ω'.

- ***Evaluation of SH coefficients.*** For the chosen normalization, SHs obey the following orthogonality relationship

$$\int \mathcal{Y}_{lm}(\omega)\mathcal{Y}_{l'm'}(\omega)\,\mathrm{d}\mathbb{S} = 4\pi\delta_{ll'}\delta_{mm'}, \tag{B5}$$

where $\delta_{ll'}$ and $\delta_{mm'}$ are Kronecker deltas. Using this property, SH coefficients of $f(\omega)$ are obtained as follows:

$$f_{lm} = \frac{1}{4\pi}\int f(\omega)\mathcal{Y}_{lm}(\omega)\,\mathrm{d}\mathbb{S}. \tag{B6}$$

- ***Evaluation of surface integrals on a unit sphere.*** We discretize the surface of a unit sphere using the so-called icosahedral pixelization method (*Tegmark*, 1996). It yields uniformly distributed quadrature points with equal pixel area. This makes numerical integration fairly straightforward as follows:

$$\int f(\omega)\,\mathrm{d}\mathbb{S} = \frac{4\pi}{N_\mathrm{T}}\sum_{j=1}^{N_\mathrm{T}} f(\omega_j), \tag{B7}$$

where ω_j is the centroid of the j-th pixel and N_T is the total number of pixels. Note that the factor $4\pi/N_\mathrm{T}$ represents the area of each pixel on the surface of a unit sphere.

B2 SH coefficients of some basic functions

- ***Ocean function.*** By definition, the ocean function is given by

$$\mathcal{O}(\omega) = \begin{cases} 1 & \text{if } \omega \in \mathbb{S}_\mathrm{O} \\ 0 & \text{otherwise} \end{cases},$$

where $\mathbb{S}_\mathrm{O}$ is the ocean surface domain on a unit sphere. As in equation (B1), we may write

$$\mathcal{O}(\omega) = \sum_{lm} \mathcal{O}_{lm} \mathcal{Y}_{lm}(\omega).$$

Following equations (B6) and using the definition of ocean function, we get

$$\mathcal{O}_{lm} = \frac{1}{4\pi} \int\limits_{\mathbb{S}_\mathrm{O}} \mathcal{Y}_{lm}(\omega)\,\mathrm{d}\mathbb{S}, \tag{B8}$$

where integration is performed only within the ocean surface domain. Following equation (B7), we obtain

$$\mathcal{O}_{lm} = \frac{1}{N_\mathrm{T}} \sum_{j \in \mathbb{S}_\mathrm{O}} \mathcal{Y}_{lm}(\omega_j). \tag{B9}$$

- ***Model forcing function.*** The first term in the right-hand side of equation (3) is the continental loading function or, if we may call, the model "forcing function". Let $F(\omega) = H(\omega)\mathcal{C}(\omega)$. We may write

$$F_{lm} = \frac{1}{4\pi} \int\limits_{\mathbb{S}_\mathrm{C}} H(\omega)\mathcal{Y}_{lm}(\omega)\,\mathrm{d}\mathbb{S},$$

where $\mathbb{S}_\mathrm{C}$ is the continental domain on a unit sphere. We derive $H(\omega)$ from the GRACE Stokes coefficients as detailed in Section 3. Following equation (B7), we get

$$F_{lm} = \frac{1}{N_\mathrm{T}} \sum_{j \in \mathbb{S}_\mathrm{C}} H(\omega_j)\mathcal{Y}_{lm}(\omega_j). \tag{B10}$$

- ***Global surface loading function.*** Since $L = F + \hat{S}$, we may write SH coefficients of L (equation 3) as follows:

$$L_{lm} = F_{lm} + \hat{S}_{lm}. \tag{B11}$$

B3 Some useful integrals and barystatic sea-level

- ***Ocean surface area on a unit sphere.*** Since $\mathcal{Y}_{00}(w) = 1$ (see Appendix B1), SH coefficient of the ocean function (equation B9) for $l = 0$ and $m = 0$ is given by

$$\mathcal{O}_{00} = \frac{N_\mathrm{O}}{N_\mathrm{T}} \equiv \frac{1}{4\pi}\left[\left(\frac{4\pi}{N_\mathrm{T}}\right) N_\mathrm{O}\right], \tag{B12}$$

where N_O is the number of pixels in the ocean surface domain $\mathbb{S}_\mathrm{O}$. Since the term enclosed by parentheses represents the area of each pixel, the total area of ocean surface (i.e., N_O times the pixel area) on a unit sphere is given by

$$\int \mathcal{O}(\omega)\,\mathrm{d}\mathbb{S} = 4\pi\,\mathcal{O}_{00}. \tag{B13}$$

- ***Continental water volume on a unit sphere.*** SH coefficient of the forcing function (B10) for $l = m = 0$ is given by

  $$F_{00} = \frac{1}{N_{\mathrm{T}}} \sum_{j \in \mathbb{S}_{\mathrm{C}}} H(\omega_j) \equiv \frac{1}{4\pi} \sum_{j \in \mathbb{S}_{\mathrm{C}}} \left[\left(\frac{4\pi}{N_{\mathrm{T}}} \right) H(\omega_j) \right]. \tag{B14}$$

  Since the term enclosed by parentheses represents the area of each pixel, the sum of the bracketed term over $\mathbb{S}_{\mathrm{C}}$ essentially yields the total continental water volume. Consequently, we may write

  $$\int H(\omega)\mathcal{C}(\omega)\,\mathrm{d}\mathbb{S} = 4\pi\, F_{00}. \tag{B15}$$

- ***Barystatic sea-level.*** Using equations (A1), (A2), (B13), and (B15), we get

  $$E = -\frac{F_{00}}{\mathcal{O}_{00}}. \tag{B16}$$

B4 SH coefficients appearing in the sea-level equation

- ***The coefficient*** $\hat{E}_{lm}$**.** This coefficient is used as the first guess solution of $\hat{S}_{lm}$ (equation 8) and remains unchanged during the recursive process. Recalling that $\hat{E} = \mathcal{O}E$ and that E is a spatial invariant, we may write

  $$\hat{E}_{lm} = \frac{1}{4\pi} E \int \mathcal{O}(\omega)\mathcal{Y}_{lm}(\omega)\,\mathrm{d}\mathbb{S}.$$

  Noting that the integral is equivalent to $4\pi\mathcal{O}_{lm}$ (cf. equation B6) and using equation (B16), we get

  $$\hat{E}_{lm} = -\frac{F_{00}}{\mathcal{O}_{00}}\mathcal{O}_{lm}. \tag{B17}$$

- ***Other hatted coefficients.*** All of the coefficients appearing in equation (8) may be evaluated in a similar manner. Consider $\hat{X}_{lm}$, for example. Recalling the definition that $\hat{X} = \mathcal{O}X$ and following equation (B6), we may write

  $$\hat{X}_{lm} = \frac{1}{4\pi} \int \mathcal{O}(\omega)X(\omega)\mathcal{Y}_{lm}(\omega)\,\mathrm{d}\mathbb{S}.$$

  Using the definition of ocean function and expanding $X(\omega)$ as in equation (B1), we get

  $$\hat{X}_{lm} = \frac{1}{4\pi} \int_{\mathbb{S}_{\mathrm{O}}} \left[\sum_{pq} X_{pq}\mathcal{Y}_{pq}(\omega) \right] \mathcal{Y}_{lm}(\omega)\,\mathrm{d}\omega.$$

  Following equation (B7), we evaluate the integral as follows

  $$\hat{X}_{lm} = \frac{1}{N_{\mathrm{T}}} \sum_{j \in \mathbb{S}_{\mathrm{O}}} \left[\sum_{pq} X_{pq}\mathcal{Y}_{pq}(\omega_j) \right] \mathcal{Y}_{lm}(\omega_j). \tag{B18}$$

- ***The coefficient*** X_{pq}**.** By definition, $X = \Phi_{\mathrm{g}}/g$. Using equations (A3) and (A4), we may write

  $$X(\omega) = \frac{3\rho_w}{4\pi\rho_e} \int \sum_{p=0}^{\infty} (1 + k'_p)\, P_p(\cos\alpha)\, L(\omega')\,\mathrm{d}\mathbb{S}',$$

Using the SH addition theorem (equation B4) and expanding $L(\omega')$ as in equation (B1), we get

$$X(\omega) = \frac{3\rho_w}{4\pi\rho_e} \int \sum_{pq} \left\{ \frac{1+k'_p}{2p+1} \mathcal{Y}_{pq}(\omega)\mathcal{Y}_{pq}(\omega') \right\} \sum_{p'q'} L_{p'q'} \mathcal{Y}_{p'q'}(\omega')\,\mathrm{d}\mathbb{S}',$$

or,

$$X(\omega) = \frac{3\rho_w}{4\pi\rho_e} \sum_{pq} \sum_{p'q'} \frac{1+k'_p}{2p+1} L_{p'q'} \mathcal{Y}_{pq}(\omega) \int \mathcal{Y}_{pq}(\omega')\mathcal{Y}_{p'q'}(\omega')\,\mathrm{d}\mathbb{S}'$$

Using the SH orthogonality relationship (equation B5), we get

$$X(\omega) = \frac{3\rho_w}{\rho_e} \sum_{pq} \frac{1+k'_p}{2p+1} L_{pq} \mathcal{Y}_{pq}(\omega). \tag{B19}$$

Using equations (B6) and (B19), SH coefficients X_{pq} are given by

$$X_{pq} = \frac{3\rho_w}{4\pi\rho_e} \int \sum_{p'q'} \left\{ \frac{1+k'_{p'}}{2p'+1} L_{p'q'} \mathcal{Y}_{p'q'}(\omega) \right\} \mathcal{Y}_{pq}(\omega)\,\mathrm{d}\mathbb{S}.$$

Rearranging terms and applying the orthogonality relationship (equation B5), we obtain

$$X_{pq} = \frac{3\rho_w}{\rho_e} \frac{1+k'_p}{2p+1} L_{pq}. \tag{B20}$$

- ***The coefficient*** Y_{pq}**.** By definition, $Y = \Phi_\mathrm{r}/g$. Using equations (A5) and (B6), SH coefficients Y_{pq} are given by

$$Y_{pq} = \frac{1}{4\pi g} \int \left[\Lambda_{00}\mathcal{Y}_{00}(\omega) + \sum_{2q'} (1+k_2)\Lambda_{2q'}\mathcal{Y}_{2q'}(\omega) \right] \mathcal{Y}_{pq}(\omega)\,\mathrm{d}\mathbb{S}.$$

Rearranging terms and applying the orthogonality relationship (equation B5), we get

$$Y_{pq} = \frac{\Lambda_{00}}{g} \delta_{p0}\delta_{q0} + \frac{(1+k_2)\Lambda_{2q}}{g} \delta_{p2}. \tag{B21}$$

- ***The coefficient*** P_{pq}**.** By definition, $P = -U_\mathrm{g}$. Using equations (A3) and (A4) and following the procedure to derive X_{pq} (equation B20), we obtain

$$P_{pq} = -\frac{3\rho_w}{\rho_e} \frac{h'_p}{2p+1} L_{pq}. \tag{B22}$$

- ***The coefficient*** Q_{pq}**.** By definition, $Q = -U_\mathrm{r}$. Using equation (A5) and following the procedure to derive Y_{pq} (equation B21), we get

$$Q_{pq} = -\frac{h_2\Lambda_{2q}}{g} \delta_{p2}. \tag{B23}$$

- ***The coefficient*** C_{pq}**.** By definition, $C = E - \langle \Phi/g - U \rangle \equiv E - \langle X + P + Y + Q \rangle$. Using equations (A5), (B19) and similar equations for P, we may write

$$C = E - \frac{1}{4\pi \mathcal{O}_{00}} \int\limits_{\mathbb{S}_O} \left[\frac{3\rho_w}{\rho_e} \sum_{pq} \frac{1+k'_p-h'_p}{2p+1} L_{pq}\mathcal{Y}_{pq}(\omega) + \frac{1}{g}\left\{ \Lambda_{00}\mathcal{Y}_{00}(\omega) + \sum_{2q}(1+k_2-h_2)\Lambda_{2q}\mathcal{Y}_{2q}(\omega)\right\}\right] \mathrm{d}\mathbb{S}.$$

Using equations (B8) and (B16), we get

$$C = -\frac{F_{00}}{\mathcal{O}_{00}} - \frac{3\rho_w}{\rho_e \mathcal{O}_{00}} \sum_{pq}\frac{1+k'_p-h'_p}{2p+1}L_{pq}\mathcal{O}_{pq} - \frac{\Lambda_{00}}{g} - \frac{1}{g\mathcal{O}_{00}}\sum_{2q}(1+k_2-h_2)\Lambda_{2q}\mathcal{O}_{2q}. \tag{B24}$$

Note that C and all of the right-hand side terms are spatially invariant. Using equations (B6) and (B24), we get

$$C_{pq} = -\frac{1}{4\pi}\left[\frac{F_{00}}{\mathcal{O}_{00}} + \frac{3\rho_w}{\rho_e\mathcal{O}_{00}}\sum_{p'q'}\frac{1+k'_{p'}-h'_{p'}}{2p'+1}L_{p'q'}\mathcal{O}_{p'q'} + \frac{\Lambda_{00}}{g} + \frac{1}{g\mathcal{O}_{00}}\sum_{2q'}(1+k_2-h_2)\Lambda_{2q'}\mathcal{O}_{2q'}\right]\int \mathcal{Y}_{pq}(\omega)\,\mathrm{d}\mathbb{S}.$$

Since $\mathcal{Y}_{00}(\omega) = 1$, we introduce a virtual expression $\mathcal{Y}_{00}(\omega)$ inside the integral and use equation (B5) to find

$$C_{pq} = -\delta_{p0}\delta_{q0}\left[\frac{F_{00}}{\mathcal{O}_{00}} + \frac{3\rho_w}{\rho_e\mathcal{O}_{00}}\sum_{p'q'}\frac{1+k'_{p'}-h'_{p'}}{2p'+1}L_{p'q'}\mathcal{O}_{p'q'} + \left\{\frac{\Lambda_{00}}{g} + \frac{1}{g\mathcal{O}_{00}}\sum_{2q'}(1+k_2-h_2)\Lambda_{2q'}\mathcal{O}_{2q'}\right\}\right]. \tag{B25}$$

The terms inside the braces vanish when rotational feedback is not included. Note that the first term in right-hand side of equation (B21) and the first term inside the braces above cancel out while solving equation (9). It is, however, important to consider these terms explicitly for a clean isolation of SH coefficients of the desired fields.

Author contributions. S.A. and E.R.I. conceived the research and wrote the first draft of the manuscript. S.A. formulated sea-level solver, with help of E.R.I., and led the calculations, with help of F.W.L. (on estimating degree 1 Stokes coefficients) and T.F. and L.C. (on uncertainty quantification). All authors contributed to the analysis of the results and to the writing and editing of the manuscript.

Competing interests. The authors declare that they have no competing interests.

Acknowledgements. This research was carried out at the Jet Propulsion Laboratory, California Institute of Technology, under a contract with National Aeronautics and Space Administration, and was primarily funded through the JPL Research, Technology & Development Program (#01-STCR-R.17.235.118; 2017-2019) and through the NASA Sea-Level Change Science Team (#509496.02.08.10.65; 2018-2020).

References

Adhikari, S. and E.R. Ivins: Climate-driven polar motion: 2003-2015, *Science Advances, 2*, e1501693, 2016.

Adhikari, S., E.R. Ivins and E. Larour: ISSM-SESAW v1.0: mesh-based computation of gravitationally consistent sea level and geodetic signatures caused by cryosphere and climate driven mass change, *Geosci. Model Dev., 9*, 9769–9816, 2016.

Adhikari, S., E.R. Ivins, T. Frederikse, F.W. Landerer and L. Caron: Spherical harmonic coefficients of relative sea-level, geoid height change, and bedrock motion derived from the Release-06 GRACE Level-2 monthly Stokes coefficients, *Harvard Dataverse, V1*, doi: 10.7910/DVN/8UC8IR, 2019.

Bettadpur, S.: Gravity Recovery and Climate Experiment Level - 2 Gravity Field Product User Handbook, *GRACE 327-734 (CSR-G-03-01) (Rev 4.0, April 25, 2018)*, podaac.jpl.nasa.gov/allData/grace/docs/L2-UserHandbook_v4.0.pdf, 2018.

Bilbao, R.A., J.M. Gregory and N. Bouttes: Analysis of the regional pattern of sea level change due to ocean dynamics and density change for 1993–2099 in observations and CMIP5 AOGCMs, *Climate Dynamics, 45*, 2647–2666, 2015.

Caron, L., E.R. Ivins, E. Larour, S. Adhikari, J. Nilsson, and G. Blewitt: GIA model statistics for GRACE hydrology, cryosphere and ocean science, *Geophys. Res. Lett., 45*, 2018.

Chambers, D.P.: Evaluation of new GRACE time-variable gravity data over the ocean, *Geophys. Res. Lett., 33*, L17603, 2006.

Chambers, D.P. and J.K. Willis: Analysis of large-scale ocean bottom pressure variability in the North Pacific, *J. Geophys. Res., 113*, C11003, 2008.

Cheng, M.K., J.C. Ries and B.D. Tapley: Variations of the Earth's figure axis from satellite laser ranging and GRACE, *J. Geophys. Res., 116*, B01409, 2011.

Cheng, M.K., J.C. Ries and B.D. Tapley: Geocenter variations from analysis of SLR data, in *Reference Frames for Applications, Geosciences, Int. Assoc. of Geod. Symp., vol. 138*, ed. Z. Altamimi and X. Collilieux, 19–25, Springer, Berlin, 2013.

Clark, J.A., P.E. Haidle and N.L. Cunningham: Comparison of satellite altimetry to tide gauge measurement of sea level: Predictions of glacio-isostatic adjustment, *J. Climate, 15*, 22, 3291–3300, 2002.

Davis, J.L. and N.T. Vinogradova: Causes of accelerating sea-level on the East Coast of North America, *Geophys. Res. Lett., 44*, 2017.

Desai, S.D.: Observing the pole tide with satellite altimetry, *J. Geophys. Res., 107(C11)*, 3186, 2002.

Desai, S.D. and D.-N. Yuan: Application of the convolution formalism to the ocean tide potential: Results from the Gravity Recovery and Climate Experiment (GRACE), *J. Geophys. Res., 111, C06023*, 2006.

Desai, S.D., J. Wahr, and B. Beckley,: Revisiting the pole tide for and from satellite altimetry. *J. Geod., 89*, 1233–1243, doi:10.1007/s00190-015-0848-7, 2015.

Dieng, H.B., A. Cazenave, K. von Schuckmann, M. Ablain and B. Meyssignac: Sea level budget over 2005–2013: missing contributions and data errors, *Ocean Sci., 11*, 789–802, 2015.

Dobslaw, H., I. Bergmann-Wolf, R. Dill, L. Poropat, M. Thomas, C. Dahle, S. Esselborn, R. Konig and F. Flechtner: A new high-resolution model of non-tidal atmosphere and ocean mass variability for de-aliasing of satellite gravity observations: AOD1B RL06, *Geophys. J. Int., 211*, 263–269, 2017.

Farrell, W.E. and J.A. Clark: On postglacial sea level, *Geophys. J. Roy. Astr. S., 46*, 647–667, 1976.

Fasullo, J.T. and R. S. Nerem: Altimeter-era emergence of the patterns of forced sea-level rise in climate models and implications for the future, *Proceedings of the National Academy of Sciences, 115*, 12944–12949, 2018.

Frederikse, T., S. Jevrejeva, R.E.M. Riva and S. Dangendorf: A consistent sea-level reconstruction and its budget on basin and global scales over 1958-2014, *Journal of Climate, 31*, 1267–1280, 2018.

Galassi, G. and G. Spada: Tide gauge observations in Antarctica (1958–2014) and recent ice loss, *Antarctic Science, 29*, 369–381, 2017.

Gaultier, L., Ubelmann, C. and Fu, L-L.: The challenge of using future SWOT data for oceanic field reconstruction, *J. Atmospheric Oceanic Tech., 33*, 119–126, doi:10.1175/JTECH-D-15-0160.1, 2016.

Han, S.-C., J. Sauber and F. Pollitz: Coseismic compression/dilatation and viscoelastic uplift/subsidence following the 2012 Indian Ocean earthquakes quantified from satellite gravity observations, *Geophys. Res. Lett., 42*, 3764–3722, 2015.

Han, S.-C., J. Sauber and F. Pollitz: Postseismic gravity change after the 2006–2007 great earthquake doublet and constraints on the asthenosphere structure in the central Kuril Islands, *Geophys. Res. Lett., 43*, 3169–3177, 2016.

Haubrich, R. and W. Munk: The pole tide, *J. Geophys. Res., 64*, 2373–2388, 1958.

Hirschi, M. and S.I. Seneviratne: Basin-scale water-balance dataset (BSWB): an update, *Earth Syst. Sci. Data, 9*, 251–258, 2017.

Hsu, C.-W. and I. Velicogna: Detection of sea level fingerprints derived from GRACE gravity data, *Geophys. Res. Lett., 44*, 8953–8961, 2017.

Ivins, E.R., M.M. Watkins, D-N. Yuan, R. Dietrich, G. Casassa and A. Rülke: On-land ice loss and glacial isostatic adjustment at the Drake Passage: 2003–2009, *J. Geophys. Res., 116*, B02403, 2011.

Ivins, E.R., T.S. James, J. Wahr, E.J.O. Schrama, F.W. Landerer and K.M. Simon: Antarctic contribution to sea-level rise observed by GRACE with improved GIA correction, *J. Geophys. Res., 118*, 3126-3141, 2013.

Johnson, G.F. and D.P. Chambers: Ocean bottom pressure seasonal cycles and decadal trends from GRACE release-05: Ocean circulation implications. *J. Geophys. Res., 118*, 4228–4240, 2013.

Jacob, T., J. Wahr, W.T. Pfeffer and S. Swenson: Recent contributions of glaciers and ice caps to sea level rise. *Nature, 482*, 514–518, 2012.

King, M.A. and A. Santamaría-Gómez: Ongoing deformation of Antarctica following recent Great Earthquakes, *Geophys. Res. Lett., 43*, 1918–1927, 2016.

Lambeck, K.: *The Earth's Variable Rotation: Geophysical Causes and Consequnces*, Cambridge Univ. Press, Cambridge, UK, pp. 449, 1981.

Lambert, A. and C. Beaumont: Nano-variations in gravity due to seasonal groundwater movements: implications for gravitational detection of tectonic movements, *J. Geophys. Res., 82*, 297–306, 1977.

Lange, H., G. Casassa, E. R. Ivins, L. Schröder, M. Fritsche, A. Richter, A. Groh and R. Dietrich,: Observed crustal uplift near the Southern Patagonian Icefield constrains improved viscoelastic Earth models, *Geophys. Res. Lett., 41,* 805–812, doi:10.1002/2013GL058419, 2014.

Landerer, F.W. and S.C. Swenson: Accuracy of scaled GRACE terrestrial water storage estimates, *Water Resour. Res., 48*, W04531, 2012.

Landerer, F.W., D.N. Wiese, K. Bentel, C. Böning and M.M. Watkins: North Atlantic meridional overturning circulation variations from GRACE ocean bottom pressure anomalies, *Geophys. Res. Lett., 42*, 8114–8121, 2015.

Larour, E., E.R. Ivins and S. Adhikari: Should coastal planners have concern over where land ice is melting? *Sci. Adv., 3*, e1700537, 2017.

Lickley, M.J., C.C. Hay, M.E. Tamisiea and J.X. Mitrovica: Bias in estimates of global mean sea level change inferred from satellite altimetry. *Journal of Climate, 31, (13)*, 5263–5271, 2018.

Luthcke, S.B., T.J. Sabaka, B.D. Loomis, A.A. Arendt, J.J. McCarthy and J. Camp: Antarctica, Greenland and Gulf of Alaska land-ice evolution from an iterated GRACE global mascon solution *J. Glaciology, 59*, 613–631, 2013.

Mazloff, M.R. and C. Böning: Rapid variability of Antarctic Bottom Water transport into the Pacific Ocean inferred from GRACE, *Geophys. Res. Lett., 43*, 3822–3829, 2016.

Milne, G.A. and J. Mitrovica: Postglacial sea-level change on a rotating Earth, *Geophys. J. Int., 133*, 1–19, 1998.

Mitrovica, J.X. and W.R. Peltier: On post-glacial geoid subsidence over the equatorial ocean, *J. Geophys. Res., 96*, 20053–20071, 1991.

Mitrovica, J.X., M.E. Tamisiea, J.L. Davis and G.A. Milne: Recent mass balance of polar ice sheets inferred from patterns of global sea-level change, *Nature, 409*, 1026–1029, 2001.

Mitrovica, J.X., C.C. Hay, R.E. Kopp, C . Harig and K. Latychev: Quantifying the sensitivity of sea level change in coastal localities to the geometry of polar ice mass flux, *J. Climate, 31*, 3701–3709, 2018.

Müller, F.L., C. Wekerle, D. Dettmering, M. Passaro, W. Bosch and F. Seitz: Dynamic ocean topography of the Greenland Sea: A comparison between satellite altimetry and ocean modeling, *The Cryosphere Discuss.*, doi:10.5194/tc-2018-184, 2018.

Nield, G.A., P. L. Whitehouse, W. van der Wal, B. Blank, J.P. O'Donnell and G. W. Stuart: The impact of lateral variations in lithospheric thickness on glacial isostatic adjustment in West Antarctica, *Geophys. J. Int., 214*, 811–824, doi:10.1093/gji/ggy158, 2018.

Peltier, W.R.: Dynamics of the Ice Age Earth, *Advances in Geophysics, 24,* 1–146, 1982.

Piecuch, C.G., P.R. Thompson and K.A. Donohue: Air pressure effects on sea level changes during the twentieth century, *J. Geophys. Res., 121*, 7917–7930, 2016.

Rapp, R.H.: The determination of geoid undulations and gravity anomalies from SEASAT altimeter data, *J. Geophys. Res., 88*, 1552–1562, 1983.

Rietbroek, R., S.-E. Brunnabend, J. Kusche and J. Schröter: Resolving sea level contributions by identifying fingerprints in time-variable gravity and altimetry, *J. Geodynamics, 59–60*, 72–81, 2012.

Rignot, E., I. Velicogna, M.R. van den Broeke, A. Monaghan and J. Lenaerts: Acceleration of the contribution of the Greenland and Antarctic ice sheets to sea level rise, *Geophys. Res. Lett., 38*, L05503, 2011.

Riva, R.E.M., J.L. Bamber, D.A. Lavallée and B. Wouters: Sea-level fingerprint of continental water and ice mass change from GRACE, *Geophys. Res. Lett., 37*, L19605, 2010.

Rodell, M. and 22 others: The observed state of the water cycle in the early Twenty-First Century, *J. Climate, 28*, 8289–8317, 2015.

Save, H., S. Bettadpur and B.D. Tapley: High-resolution CSR GRACE RL05 mascons, *J. Geophys. Res., 121*, 7547–7569, 2016.

Saynisch, J., I. Bergmann-Wolf and M. Thomas: Assimilation of GRACE-derived oceanic mass distributions with a global ocean circulation model, *J. Geodesy, 89,* 121–139, doi:10.1007/s00190-014-0766-0, 2015.

Schrama, E.J.O., B. Wouters and R. Rietbroek: A mascon approach to assess ice sheet and glacier mass balances and their uncertainties from GRACE data. *J. Geophys. Res., 119*, 6048–6066, 2014.

Shepherd A., and the IMBIE-2 Team: Mass balance of the Antarctic Ice Sheet from 1992 to 2017, *Nature, 558*, 219–222, 2018.

Simon, K.M., R.E.M. Riva, M. Kleinherenbrink and T. Frederikse: The glacial isostatic adjustment signal at present day in northern Europe and the British Isles estimated from geodetic observations and geophysical models, *Solid Earth, 9*, 777–795, 2018.

Spada, G.: Glacial isostatic adjustment and contemporary sea level rise: An overview, *Surv. Geophys., 38*, 153–185, 2017.

Spada, G. and G. Galassi: Spectral analysis of sea level during the altimetry era, and evidence for GIA and glacial melting fingerprints, *Global and Planetary Change, 143*, 34–49, 2016.

Stammer, D. and others: Accuracy assessment of global barotropic ocean tide models, *Rev. Geophys., 52*, doi:10.1002/2014RG000450, 2014.

Sterenborg. M.G., E. Morrow and J.X. Mitrovica: Bias in GRACE estimates of ice mass change due to accompanying sea-level change, *J. Geodesy, 87*, 387–392, 2013.

Stocchi, P. and G. Spada: Influence of glacial isostatic adjustment upon current sea level variations in the Mediterranean, *Tectonophysics, 474*, 56–68, 2009.

Swenson, S., D. Chambers and J. Wahr: Estimating geocenter variations from a combination of GRACE and ocean model output, *J. Geophys. Res., 113*, B08410, 2008.

Tamisiea, M.E.: Ongoing glacial isostatic contributions to observations of sea level change, *Geophys. J. Int., 186*, 1036–1044, 2011.

Tamisiea M.E., C.W. Hughes, S.D.P. Williams and R.M. Bingley: Sea level: measuring the bounding surfaces of the ocean, *Phil. Trans. R. Soc. A, 372*, doi:10.1098/rsta.2013.0336, 2014.

Tapley, B.D., M.M. Watkins, F. Flechtner, C. Reigber, S. Bettadpur and 16 others, Contributions of GRACE to understanding climate change, *Nature Climate Change*, in review, 2018.

Tegmark, M.: An icosahedron-based method for pixelizing the celestial sphere, *Astrophysical J. Lett., 470*, L81–L84, 1996.

Velicogna, I.: Increasing rates of ice mass loss from the Greenland and Antarctic ice sheets revealed by GRACE, *Geophys. Res. Lett., 36*, L19503, 2009.

Wahr J.M.: Deformation induced by polar motion, *J. Geophys. Res., 90(B11)*, 9363–9368, 1985.

Wahr, J., M. Molenaar and F. Bryan: Time variability of the Earth's gravity field: Hydrological and oceanic effects and their possible detection using GRACE, *J. Geophys. Res., 103, (B12)*, 30205–30230, 1998.

Wahr, J., R.S. Nerem and S.V. Bettadpur: The pole tide and its effect on GRACE time-variable gravity measurements: Implications for estimates of surface mass variations, *J. Geophys. Res. Solid Earth, 120*, 4597–4615, 2015.

Watkins, M.M., D.N. Wiese, D.-N. Yuan, C. Böning and F.W. Landerer: Improved methods for observing Earth's time variable mass distribution with GRACE, *J. Geophys. Res., Solid Earth, 120*, 2648–2671, 2015.

WCRP Global Sea Level Budget Group: Global sea-level budget 1993–present, *Earth Syst. Sci. Data, 10*, 1551–1590, 2018.

Wiese, D.N., F.W. Landerer and M.M. Watkins: Quantifying and reducing leakage errors in the JPL RL05M GRACE mascon solution, *Water Resour. Res., 52*, 7490–7502, 2016.